Proceedings of the
Annual Stability Conference
Structural Stability Research Council
Charlotte, North Carolina, April 11-14, 2023

Response and Strength of Intermediately Stiffened Cold-Formed Steel Lipped Channel Columns Formed from 100 ksi (690 MPa) Steel

Damir Akchurin[1], Chu Ding[2], Brian Bogh[3], Shahabeddin Torabian[4], Benjamin W. Schafer[5]

Abstract

The main objective of this paper is to summarize findings of recent axial compression tests on a cold-formed lipped channel section with multiple intermediate longitudinal stiffeners in the web, a single longitudinal stiffener in the flanges, and return lips formed from high strength low-alloy steel with a yield strength of 100 ksi (690 MPa). The studied section has potential application as driven piles intended to provide support for solar array installations. The paper also provides a complete analysis of the elastic stability of the section, compression test results at three different lengths, material test results, comparison with a study investigating the axial compressive strength of advanced high-strength steel (AHSS) members, and comparison with available strength design predictions.

1. Introduction

Due to the accelerating growth of the use of renewable energy sources worldwide, the use of solar panels is rapidly increasing. According to the US Energy Information Administration, the number of residential solar panel array installations in the US rose by 34% from 2020 to 2021 [1]. Supports for ground-based solar panel arrays (Figure 1) come in a wide variety of forms, including cast-in-place concrete piers, precast concrete piers, helical (screw) piles, and driven piles [2]. Among all available options, driven piles are the least expensive and simplest to install. The use of cold-formed steel (CFS) U-, Σ-, or C-sections may have some advantages for driven piles. CFS piles are efficient with a high strength-to-weight ratio, low cost of manufacturing, and ease of fabrication. CFS has great potential to further increase material efficiency through optimization of the cross-sectional shape fabricated. In addition, several high strength ($F_y \geq 100$ ksi (690 MPa)) sheet steels are now available, further opening up the opportunity for further optimization. Significant research efforts have been devoted to seeking more materially efficient CFS sections using optimization [3]–[6].

[1] Graduate Research Assistant, Department of Civil and Systems Engineering, Johns Hopkins University, akchurd1@jhu.edu
[2] Former Graduate Research Assistant, Department of Civil and Systems Engineering, Johns Hopkins University, cding6@jhu.edu
[3] Senior Research Engineer, Verco Decking Inc., bbogh@vercodeck.com
[4] Associate Research Scientist, Department of Civil and Systems Engineering, Johns Hopkins University, torabian@jhu.edu
[5] Professor, Department of Civil and Systems Engineering, Johns Hopkins University, schafer@jhu.edu

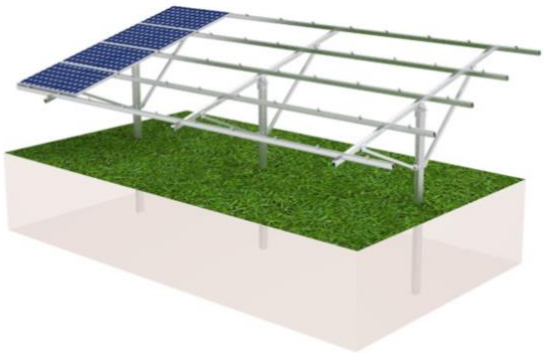

Figure 1: Rendering of a solar panel array installation supported by driven piles from [7].

The experimental study presented herein investigates the compressive buckling behavior of CFS piles formed with a lipped channel section with intermediate longitudinal stiffeners and return lips specifically designed and optimized for the purposes of being used as driven piles that provide support for solar panel array installations. The piles are made of galvanized zinc-coated high strength low-alloy (HSLA) steel with a nominal yield strength of 100 ksi (690 MPa). The study was performed by conducting a series of axial compression tests on three sets of piles with different lengths as well as tensile coupon tests to determine the material properties of the HSLA steel for further strength prediction analysis.

2. Nominal Section

The nominal section is a 6 in. wide and 4 in. deep lipped channel that includes 1 in. lips and features two intermediate flat hat-shaped stiffeners in the web, one intermediate stiffener in the flange, and return lips. The nominal thickness of the section is 0.075 in. The nominal dimensions of the section of the tested piles are provided in Figure 2.

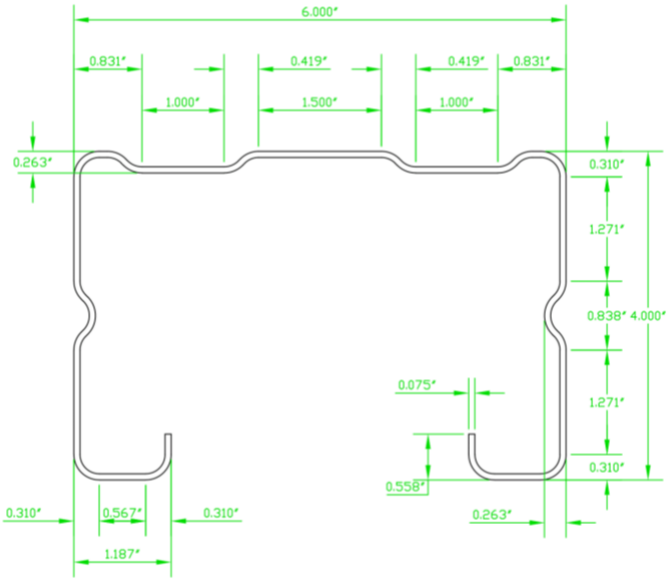

Figure 2: Nominal dimensions (in.) of nominal section of the tested piles.

3. Elastic Buckling Analysis of Nominal Section

An elastic buckling analysis (traditional signature curve only) of the nominal section, performed with an open-source elastic buckling analysis software CUFSM [8], is shown in Figure 3 along with a comparable lipped channel section with the same outer dimensions and thickness. The signature curve assumes simply-supported boundary conditions, which are different from testing conducted herein, but provides a complete picture of the cross-section stability modes expected in this section.

As can be observed from Figure 3, the critical buckling load in the local buckling mode, L, is significantly increased by the presence of the longitudinal stiffeners. Additionally, the presence of the longitudinal stiffeners results in the formation of two distortional buckling modes, D1 and D2, as compared to just one distortional buckling mode for the section with no intermediate stiffeners. Even though the first distortional buckling mode for the stiffened section, D1, is similar to the local buckling mode of the comparable unstiffened section, it is conventionally classified as a distortional buckling mode due the distortional buckling of the intermediate stiffeners on the web and flanges [9]–[11]. Lastly, the critical buckling loads in the global buckling mode, G, are practically the same as the moments of inertia for both sections are close with only a slight difference caused by the presence of stiffeners and return lips.

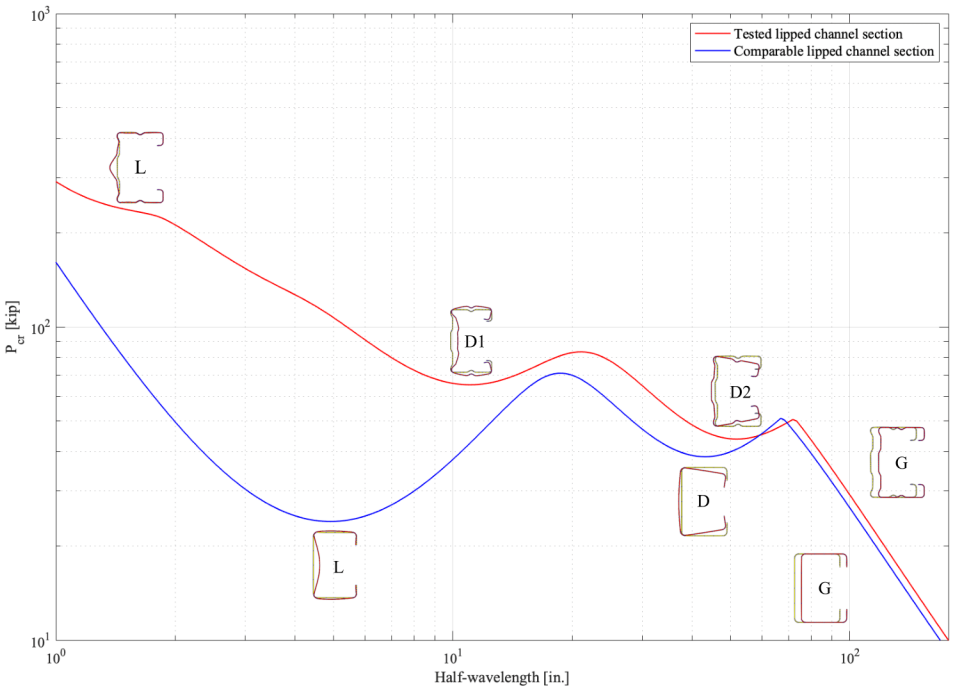

Figure 3: Comparison between the signature curves of the nominal tested section and a comparable lipped channel section with the same outer dimensions and thickness.

4. Testing Setups

Three sets of test specimens at lengths of 12 in., 24 in., and 48 in. were provided for testing under axial compression. These specific lengths where chosen based upon the results of a larger study investigating the axial compressive strength of advanced high-strength steel (AHSS) members,

conducted at the Thin-Walled Structures Laboratory at Johns Hopkins University. In general, previous work suggests 12 in.-long members primarily fail due to the local mode, 24 in.-long members may often fail due in part to the distortional mode, and 48 in.-long members are influenced in their failure by the global mode [12].

Each testing set consisted of 6 compression members of the same length, except for the testing set for 48 in.-long members, which consisted of 5 specimens. In total, 18 specimens were available for testing; 17 of those specimens were used for axial compression tests, and one 48"-long specimen was used to make coupons for tensile tests to determine the material properties of the HSLA steel. Additionally, each specimen has been laser scanned prior to testing to study the effect of geometric imperfections.

4.1 Axial Compression Testing Setup

The tests were performed on the uniaxial MTS loading rig capable of applying a compressive force of 100 kips. The test specimens were positioned between the loading platens such that the centroid of the test specimens was aligned with the centerline of the MTS loading rig to ensure a uniform and consistent compression across the cross-section as shown in Figure 4. The specimens were tested with simple steel-to-steel end bearing, no welding nor other restraint was provided between the end of the test specimens and the loading platens.

Loading was applied through the actuator below the bottom loading platen at a constant rate of 0.078 in./min. An MTS FlexTest controller was used to drive the actuator displacement and record the applied displacement via an internal linear variable differential transformer (LVDT); and the applied force via a load cell connected to the crosshead. Both displacement and force transducers are routed through a USB-based data acquisition (DAQ) system for reading, monitoring, and storing the data via LabView software.

During testing, a digital camera was set up in front of the MTS loading rig to capture images throughout the entire testing process. The camera was controlled through a tethered shooting software Canon EOS Utility. Image capture took place every 10 seconds until the testing was concluded. The images were later synchronized with the test data and turned into time-lapse videos for further visual assessment of the buckling behavior of the tested specimens.

For safety, an aluminum lateral restraint was devised and installed on the MTS loading rig as shown in Figure 4. The lateral restraint does block a portion of the specimen from direct viewing during testing but is considered necessary given the simple end bearing details of the specimen and the potential for out-of-plane movement during buckling.

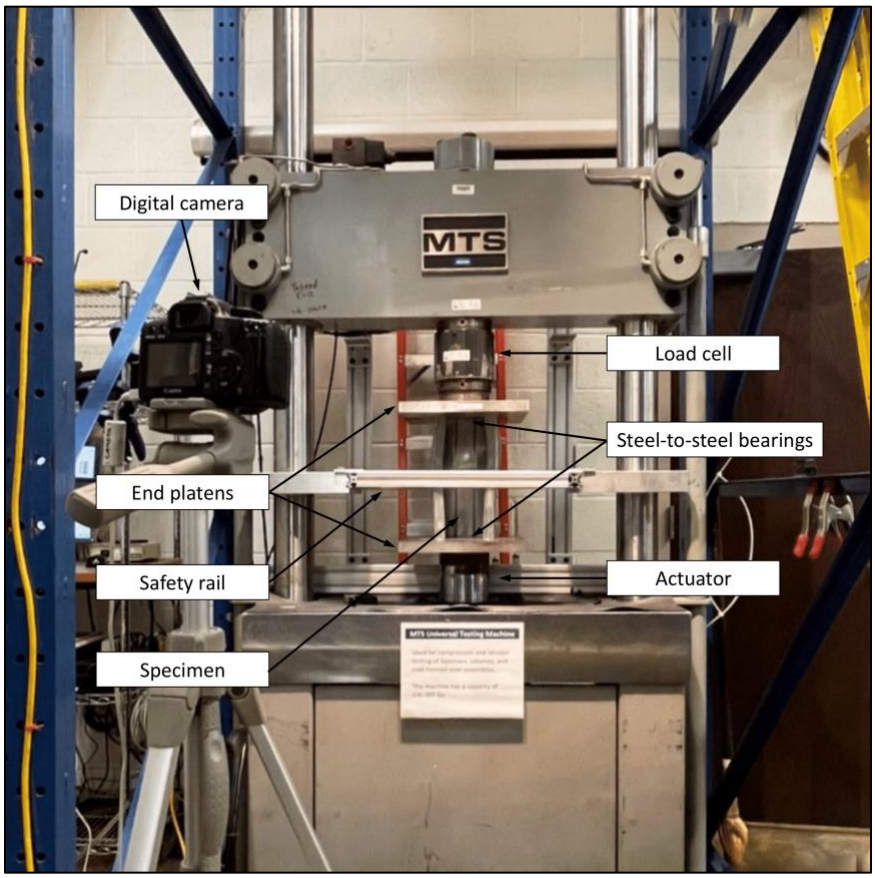

Figure 4: Axial compression testing setup.

4.2 Tensile Coupon Testing Setup

Tensile coupons were manufactured and tested in accordance with the ASTM E8/E8M – 13a standard [13]. The dimensions for the sheet-type tensile coupons manufactured and tested herein are shown in Figure 5.

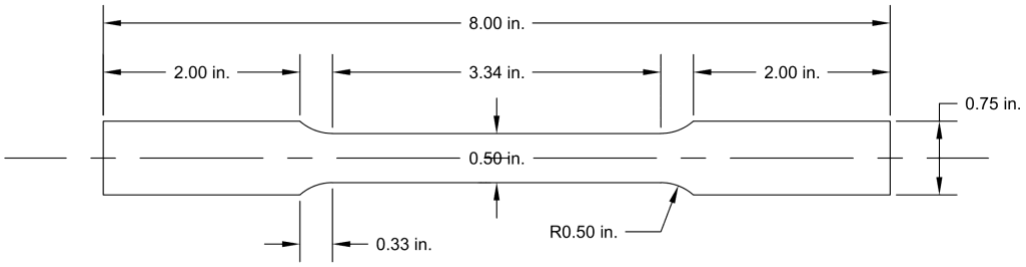

Figure 5: Dimensions of manufactured and tested tensile coupons.

Tensile coupon tests were performed on an MTS Criterion Model C43 rig capable of applying a maximum of 11 kips tensile force. A typical tensile coupon testing setup is shown in Figure 6.

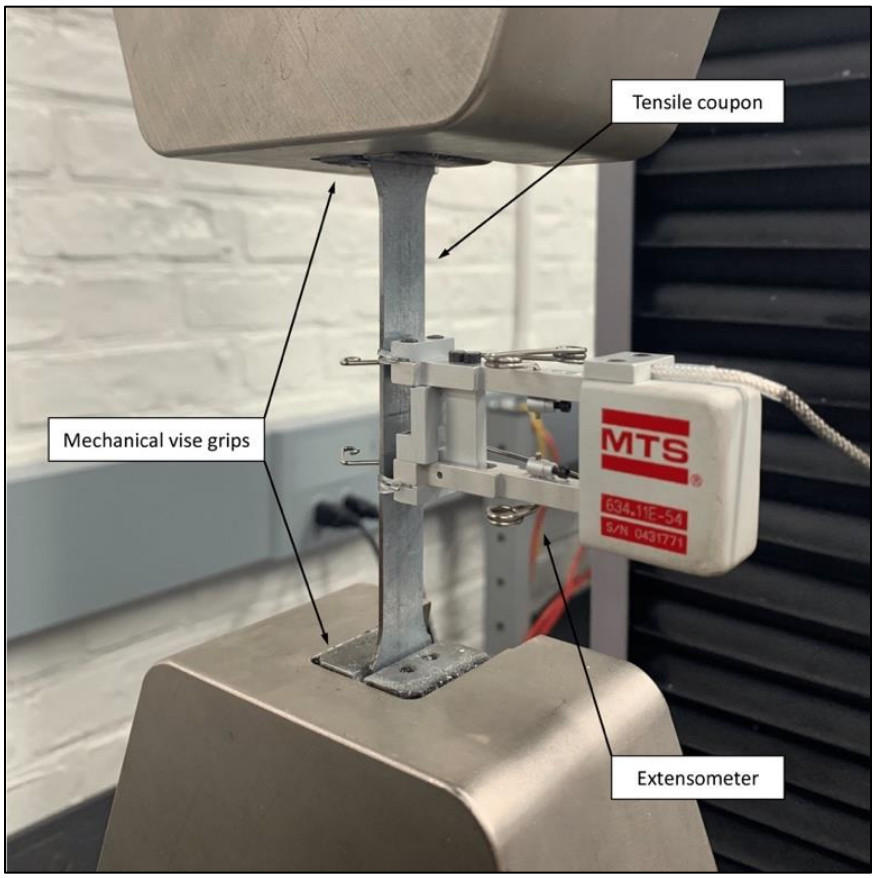

Figure 6: Tensile coupon testing setup.

The coupons were cut out from a single 48 in.-long specimen, at 7 different locations: two from each flange (FR1/FR2 (right flange) and FL1/FL2 (left flange)), one from each web stiffener (WS1 and WS2), and one from the web middle strip (W); thus, the tensile coupon test matrix consisted of 7 coupons. All coupons were cut in the longitudinal direction of the specimen. The zinc coating was stripped off the end of the coupons by submerging them in 1M HCl solution for 30 minutes to obtain the uncoated thickness of each coupon for yield strength calculations.

5. Results

5.1 Results of the Axial Compression Tests

Table 1 provides a summary of the findings from the axial compression tests with peak load and crosshead displacement at peak load values as shown, along with a categorization of the failure mechanism.

Table 1: Summary of the results of axial compression tests.

Specimen	Peak load (kip)	Crosshead displacement at peak load (in.)	Failure mechanism
12-1	85.0	0.125	Web-in, flanges-out
12-2	85.0	0.111	Web-in, flanges-out
12-3	85.5	0.131	Web-in, flanges-out
12-4	87.4	0.110	Web-in, flanges-out
12-5	84.0	0.134	Web-in, flanges-out
12-6	84.7	0.120	Web-in, flanges-out
24-1	80.3	0.134	Web-out, flanges-in
24-2	78.5	0.151	Web-out, flanges-in
24-3	80.2	0.147	Web-out, flanges-in
24-4	81.1	0.115	Web-in, flanges-out
24-5	80.7	0.120	Web-out, flanges-in
24-6	79.6	0.147	Web-out, flanges-in
48-1	76.6	0.154	Web-out, flanges-in
48-2	76.1	0.163	Web-out, flanges-in
48-3	70.6	0.212	Web-out, flanges-in
48-4	74.7	0.191	Web-out, flanges-in
48-5	72.8	0.187	Web-out, flanges-in

Note: Both web-in, flanges-out and web-out, flanges-in failure mechanisms are most compatible with the D2 buckling mode.

5.1.1 Results of the Axial Compression Tests: 12"-long specimens

Force-displacement curves for the six tested 12 in.-long specimens are shown in Figure 7. The average peak load for specimens of this length is 85.3 kips.

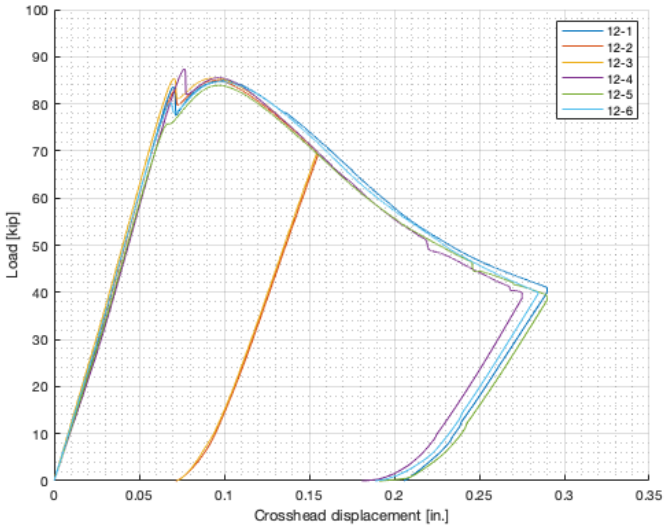

Figure 7: Force-displacement curves for 12 in.-long specimens.

Even at this short length of 12 in., the observed failure mechanism is most similar to the distortional buckling mode D2. An illustrative example of the development of a typical observed failure mechanism is shown in Figure 8. It is important to note that all 12 in.-long specimens failed in a mechanism where the web buckled inward, and the flanges buckled outward (web-in, flanges-out).

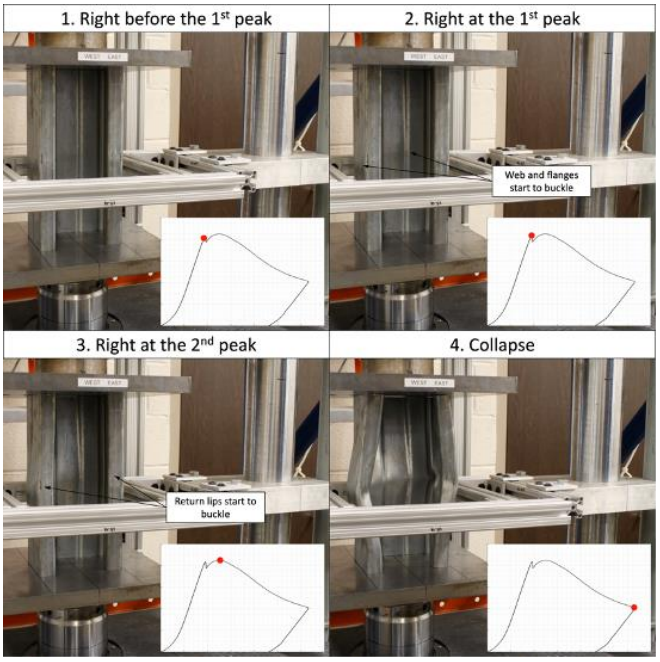

Figure 8: Progressive failure of specimen 12-1 (web-in, flanges-out) at different stages: right before the 1st peak, right at the 1st peak, right at the 2nd peak, and full collapse.

From Figure 7 it can be observed that the force-displacement curves have two distinct peaks. During the testing process, it was noted that the first peak is always associated with the buckling of the web and flanges, and the second peak is associated with the buckling of the return lips. This may be understood as a mechanism associated with the buckling mode D1 followed by a mechanism associated with the buckling mode D2.

5.1.2 Results of the Axial Compression Tests: 24"-long specimens

From the force-displacement curves for the six tested 24 in.-long specimens shown in Figure 9 it can be determined that the average peak load is 80.1 kips. Again, all the test specimens have failed in mechanism associated with distortional buckling D2. Five out of six tested 24 in.-long members have failed in web-out, flanges-in mode, and one of them (specimen 24-4) have failed in web-in, flanges-out mode similar to all the 12 in.-long members.

It can also be observed from Figure 9, that the force-displacement curves have two distinct peaks, and their basic nature is the same as the shorter 12 in.-long members: the first peak is associated with the buckling of the web and flanges, and the second peak is associated with the buckling of the return lips. Again, this may be understood as a mechanism associated with the buckling mode D1 followed by a mechanism associated with the buckling mode D2; however, in the case of 24 in.-long specimens, rotation of the flanges occurs earlier than in the 12 in.-long specimens and more of the overall deformation is associated with the buckling mode D2. An illustrative example of a development of a typical web-out, flanges-in distortional buckling mode, as observed in specimen 24-1 is shown in Figure 10.

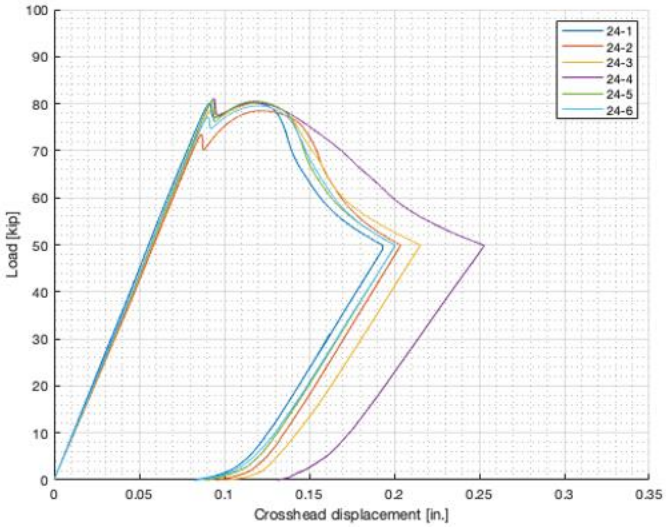

Figure 9: Force-displacement curves for 24 in.-long specimens.

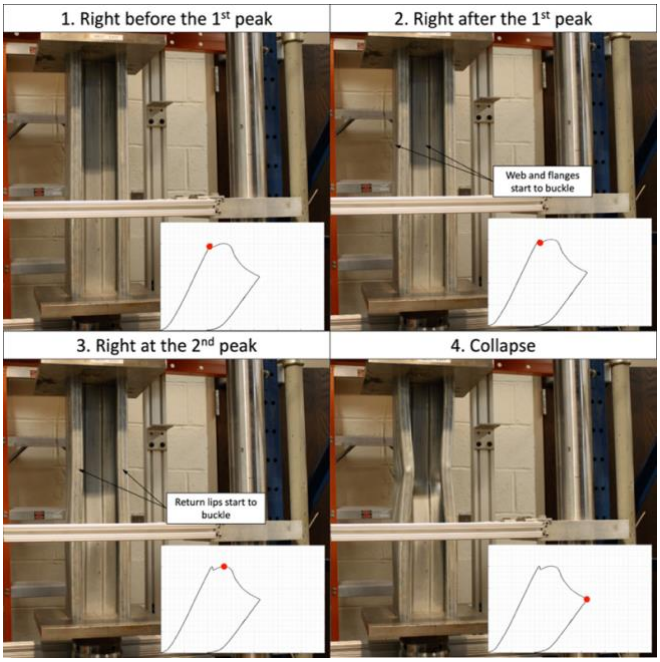

Figure 10: Progressive failure of specimen 24-1 (web-out, flanges-in) at different stages: right before the 1st peak, right after the 1st peak, right at the 2nd peak, and full collapse.

5.1.3 Results of the Axial Compression Tests: 48"-long specimens

From the force-displacement curves for the six tested 48 in.-long specimens, as shown in Figure 11, it can be determined that the average peak load is 74.1 kips.

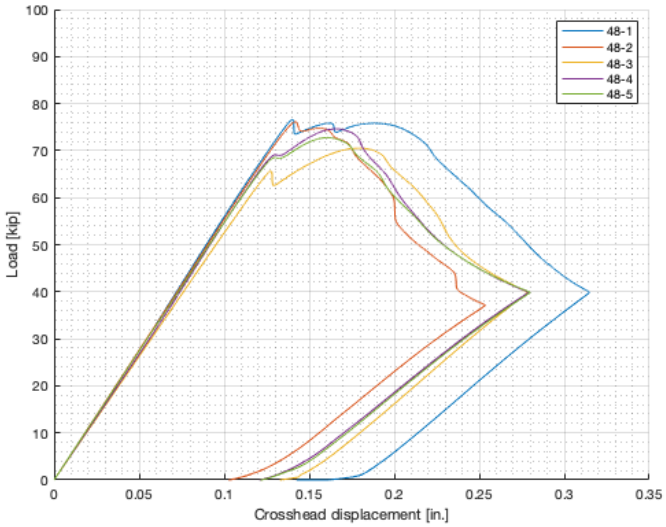

Figure 11: Force-displacement curves for 48 in.-long specimens.

It may be observed from Figure 11, that the force-displacement curves have three peaks with specimen 48-1 having the most distinct peaks: the first peak is associated with the buckling of the web and flanges at the middle of the specimen (Figure 12 (1)), the second peak is associated with the buckling of the web and flanges within the upper part of the specimen (Figure 12 (2)), and the third peak is associated with the buckling of the return lips (Figure 12 (3)). Again. this may be understood as a mechanism associated with the buckling mode D1 followed by two mechanisms along the height associated with the D2. Little to no global buckling mode G interaction is observed even in the 48 in.-long specimens.

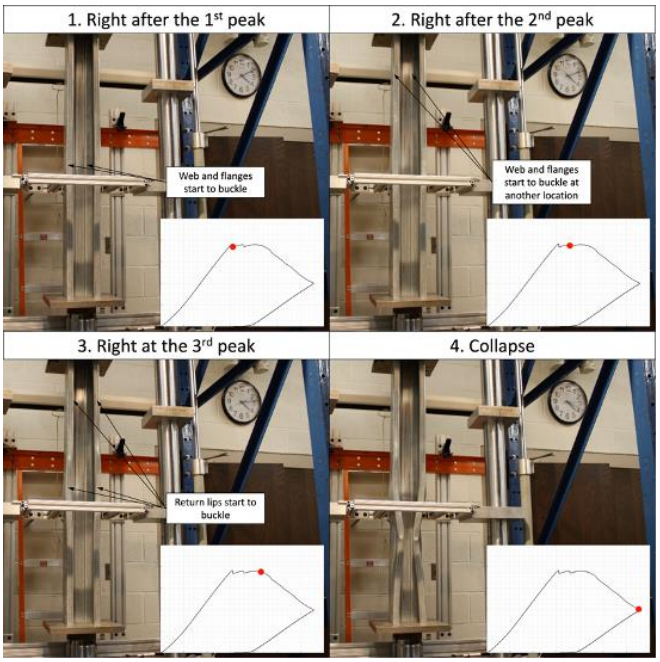

Figure 12: Progressive failure of specimen 48-1 (web-out, flanges-in) at different stages: right after the 1st peak, right after the 2nd peak, right after the 3rd peak, and full collapse.

5.2 Results of the Tensile Coupon Tests

The stress-strain curves obtained from data collected during the tensile coupon tests are shown in Figure 13. From these stress-strain results it was determined that the mean and standard deviation of the yield strength of the HSLA steel is 100.5 ksi and 1.7 ksi, respectively. The mean and standard deviation of the elastic modulus of the HSLA steel are measured as 31760 ksi and 2260 ksi based on the extensometer readings. The data collected for all coupon tests is summarized in Table 2. Only minor variation is observed in the yield strength for coupons taken from the flat and stiffeners regions indicating minimal work hardening in the section. Note, the nominal (expected) value of the yield strength was 100 ksi. In the later sections, the measured value of the yield strength and elastic modulus of the HSLA steel are used to perform preliminary strength prediction calculations.

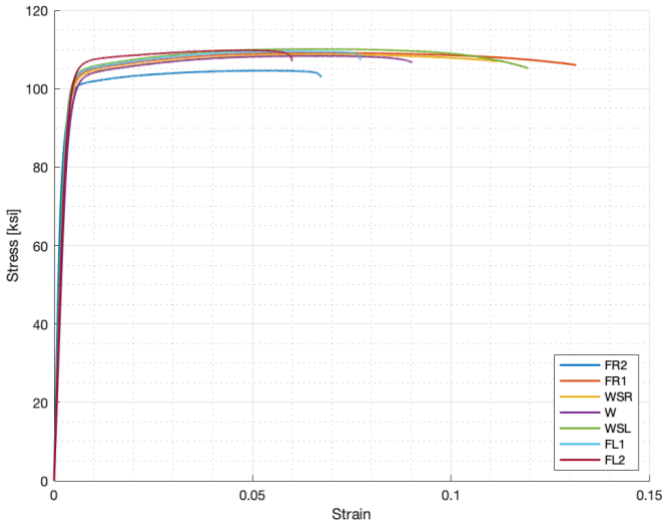

Figure 13: Stress-strain curves for HSLA steel coupon cut and manufactured from a 48"-long specimen.

Table 2: Summary of the results of the tensile coupon tests.

Specimen	**Width (in.)**	**Thickness (in.)**	E **(ksi)**	F_y **(ksi)**	F_u **(ksi)**	ε_y	ε_u	ε_f
FL2	0.500	0.080	45540.2	100.3	104.6	0.0055	0.0510	0.0673
FL1	0.501	0.076	30690.9	99.3	109.1	0.0042	0.0647	0.1316
WSL	0.502	0.077	31607.0	100.1	108.6	0.0048	0.0663	0.1117
W	0.501	0.077	28622.5	102.6	108.3	0.0053	0.0658	0.0903
WSR	0.504	0.076	35442.7	100.4	110.1	0.0051	0.0667	0.1194
FR1	0.500	0.076	32682.9	102.9	109.5	0.0053	0.0601	0.0772
FR2	0.499	0.077	31514.5	98.0	109.8	0.0051	0.0482	0.0600
Mean	0.501	0.077	31760.1	100.5	108.6	0.005	0.060	0.094
STD	0.002	0.001	2060.9	1.6	1.7	0.0004	0.007	0.025
CoV (%)	0.308	1.551	6.489	1.584	1.592	8.011	11.897	27.114

Notes: The mean and standard deviation values of the elastic modulus were calculated disregarding the specimen FL2 which demonstrated high stiffness and brittleness compared to other specimens.

6. Discussion

6.1 Geometric Imperfections: Preliminary Results

Initial geometric imperfections are known to influence strength. For this reason, test specimens were scanned prior to testing using a laser scanning machine [14] in the Thin-Walled Structures

Laboratory. Due to the geometry, each specimen was scanned twice, each time at different angle, to obtain an image of its whole point cloud, which can be used to further examine initial geometric imperfections. The process of assembling individual scans together, despite being partly automated, still requires significant manual input to obtain ideal point clouds that yield the best results. As an example of utilizing the imperfection data, we provide results of the geometric imperfections for the specimen 48-1 shown in Figure 14.

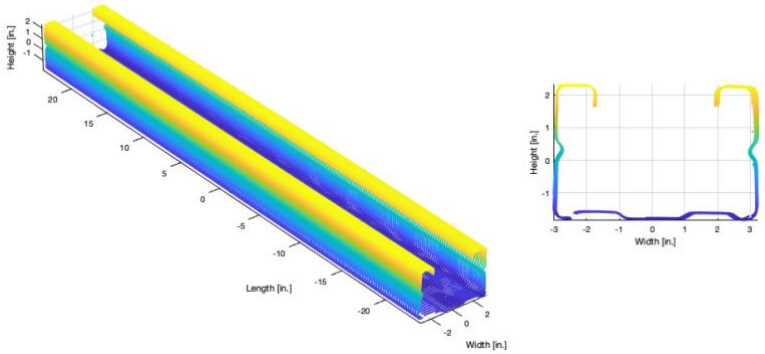

Figure 14: Point cloud for specimen 48-1.

Further processing of the obtained point clouds is to determine the contributions of the buckling modes associated with cross-sectional instabilities (L, D1, and D2 modes indicated in Figure 2) in the geometry of the specimens prior to testing. Mathematically, the problem may be formulated as follows:

$$\{D_{imp}\} = c_L\{D_L\} + c_{D1}\{D_{D1}\} + c_{D2}\{D_{D2}\} + \{R\} \tag{1}$$

where, $\{\cdot\}$ indicates a column vector and $\{D_{imp}\}$ is the measured point cloud with the nominal coordinates subtracted, $\{D_L\}$ is the L mode, $\{D_{D1}\}$ is the D1 mode, $\{D_{D2}\}$ is the D2 mode, all determined from CUFSM, $\{R\}$ is the residual error, and c_L, c_{D1}, c_{D2} are the weighting coefficients of interest for describing the initial imperfect geometry. Since the system of equations given by Eq. (1) is overdetermined, the method of least-squares was used to find the coefficients c_L, c_{D1}, and c_{D2} that minimize the residual error $\{R\}$ given by Eq. (2).

$$\{R\} = \{D_{imp}\} - (c_L\{D_L\} + c_{D1}\{D_{D1}\} + c_{D2}\{D_{D2}\}) \tag{2}$$

The results of the solution of the described minimization problem for specimen 48-1 applied cross-section by cross-section along the length are shown on Figure 15. It can be observed that compared to the modes L and D1, the distortional buckling mode D2 has the highest magnitude in the initial geometric imperfections across the whole length of the specimen. This is consistent with the observed failure mode of this specimen.

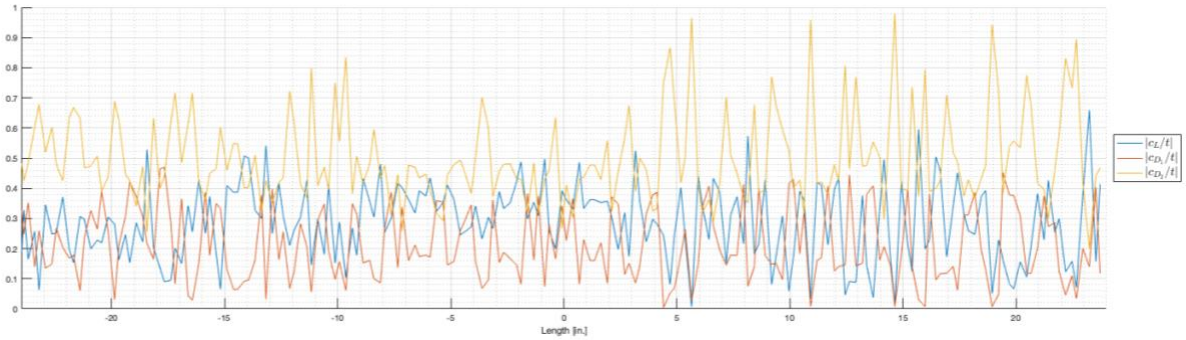

Figure 15: Magnitude of modes L, D1, D2 in the initial geometric imperfections of the specimen 48-1.

Additional data is provided in the test report [15], and in the future work, the laser scanning data can further be utilized to update the nominal dimensions to actual dimensions. In addition, dimensional tolerances and angles could all be formally quantified and compared against intended fabrication standards.

6.2 Comparison with the Direct Strength Method

In this section we provide a preliminary evaluation for strength predictions from the Direct Strength Method (DSM) in the North American Specification for Cold-Formed Steel Structural Members: AISI S100-16 [16]. The DSM strength prediction expressions combine critical buckling loads ($P_{cr\ell}, P_{crd}, P_{cre}$) with appropriate yield load (P_y) to produce axial strength capacity (P_n). Herein we use the smaller of D1 and D2 for P_{crd}. In addition, we use nominal dimensional properties; however, we use the average measured yield stress. Note, a rational argument could be made to define $P_{cr\ell}$ as the smaller of L and D1 as well in the DSM implementation – this was not pursued here.

In the work described herein, the specimens were tested with simple steel-to-steel end bearing, no welding nor other restraint was provided between the end of the test specimens and the loading platens. For the DSM solution we determine the elastic buckling loads for both upper-bound C-C (clamped-clamped) end boundary conditions and lower-bound S-S (simply supported-simply supported) end boundary conditions using CUFSM. This same approach was taken in the parallel testing on AHSS sections in [12]. The normalized elastic buckling values utilized in our calculations are provided in Table 3. Based on the elastic buckling inputs and the tested strengths the average test-to-predicted ratios in the test series are provided in Table 4.

Table 3: Normalized critical buckling loads used in DSM calculations.

Specimen length (in.)	**Boundary conditions**					
	S-S (simply supported)			**C-C (clamped)**		
	$P_{cr\ell}/P_y$	P_{crd}/P_y	P_{crg}/P_y	$P_{cr\ell}/P_y$	P_{crd}/P_y	P_{crg}/P_y
12	1.98	0.56	17.71	1.98	0.93	59.42
24	1.98	0.56	4.66	1.98	0.68	17.71
48	1.98	0.38	1.18	1.98	0.59	4.66

Table 4: Comparison of test-to-predicted strength ratios between S-S and C-C boundary conditions.

Specimen length (in.)	Boundary conditions			
	S-S (simply supported)		C-C (clamped)	
	Mean	CoV	Mean	CoV
12	**1.16**	0.014	**0.93**	0.014
24	**1.09**	0.011	**0.99**	0.011
48	**1.22**	0.033	**0.99**	0.033
All lengths	**1.16**	0.020	**0.97**	0.020

The Table 4 results indicate that DSM can adequately capture the strength of these specific complex high strength steel members. Use of the S-S assumption is conservative, and use of the C-C assumption is more reliable but modestly unconservative in this case; indicating that lift-off (warping) of the section is not a concern. Note, in plain lipped channels, the lip typically lifts off from the platen in the D buckling mode and this reduces the strength more substantially, with return lips this lift-off is mitigated significantly, and the results fall more in line with the upper-bound strength.

6.3 Comparison with AHSS Tested Specimens

The experimental study conducted herein was performed concurrently with a larger study investigating the axial compressive strength of advanced high-strength steel (AHSS) members [12]. In that study 4 in. and 6 in. deep C- and Σ-sections formed from mild steel, dual phase steel, and martensitic steels were tested on the same rig at 12 in., 24 in., and 48 in. lengths. The strength of the tests reported herein (Nucor) is compared with the AHSS tests performed as part of a National Science Foundation (NSF) project are provided in Figure 16. One can observe that the tests conducted herein are stronger than nearly all of the specimens tested in [12] and close to the capacity of the testing rig (100 kips).

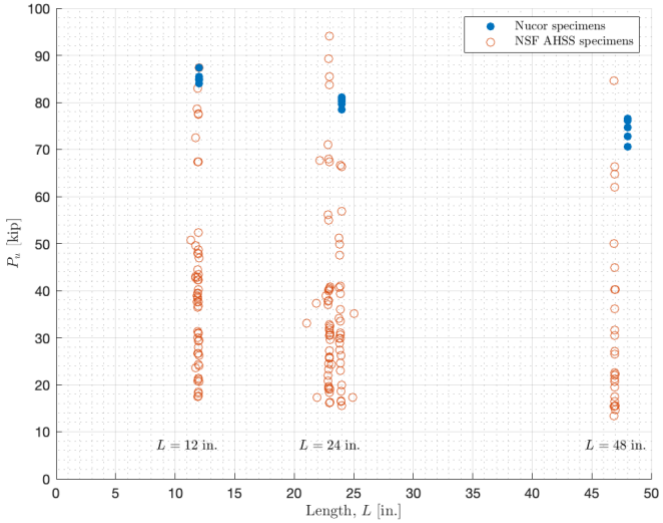

Figure 16: Comparison of observed strength of tested specimens against C- and Σ-sections from [12] tested on the same rig and with the same boundary conditions.

Additional discussion and comparison with the AHSS test data are provided in [15].

7. Conclusions

This paper presents a summary of experimental findings on the compressive strength of cold-formed high strength low-alloy steel lipped channels intended to be utilized as driven piles providing supports to solar panel array installations. The tested specimens are lipped channel sections with nominal outer cross-sectional dimensions of 6 in. wide and 4 in. deep, 1 in. lips, two intermediate flat hat-shaped stiffeners in the web, one intermediate stiffener in the flange, and return lips. The axial compression tests were conducted with simple steel-to-steel end bearings and resulted in highly repeatable strengths at all studied lengths: 12 in., 24 in., and 48 in. Mean peak strength for the shortest 12 in.-long specimens was found to be 85.3 kips, 80.1 kips for the 24 in.-long specimens, and 74.1 kips for the 48 in.-long specimens. The obtained strengths were then compared to strength predictions from the Direct Strength Method assuming either simply supported or clamped end boundary conditions. Although the test conditions only use simple steel-to-steel end bearing, the best agreement is still found when assuming clamped end boundary conditions; mean test-to-predicted strength ratio is 1.16 assuming simply supported ends and 0.97 assuming clamped ends. In addition, work to summarize measured initial geometric imperfections and comparisons against a set of companion tests using advanced high strength sheet steels are discussed.

Acknowledgements

The team would like to acknowledge Nucor Corp. for providing the specimens tested herein. The team would also like to thank lab manager Nick Logvinovsky for his technical support throughout the testing.

References

[1] L. Jamison and E. Fasching, "Record numbers of solar panels were shipped in the United States during 2021," US Energy Information Administration, Sep. 2022. [Online]. Available: https://www.eia.gov/todayinenergy/detail.php?id=53679

[2] A. J. Lutenegger, "Tension Tests on Driven Fin Piles for Support of Solar Panel Arrays," in *GeoCongress 2012*, Oakland, California, United States, Mar. 2012, pp. 305–314. doi: 10.1061/9780784412121.032.

[3] Z. Li, J. Leng, J. K. Guest, and B. W. Schafer, "Two-level optimization for a new family of cold-formed steel lipped channel sections against local and distortional buckling," *Thin-Walled Structures*, vol. 108, pp. 64–74, Nov. 2016, doi: 10.1016/j.tws.2016.07.004.

[4] D. Akchurin, C. Ding, Y. Xia, H. Blum, B. W. Schafer, and Z. Li, "Optimization of Cold-Formed Steel Members Considering Reduced Stiffness and Strength Due to Cross-Sectional Instabilities," presented at the Structural Stability Research Consortium Annual Stability Conference, Denver, CO, Mar. 2022.

[5] M. Moharrami, A. Louhghalam, and M. Tootkaboni, "Optimal Folding of Cold Formed Steel Cross Sections Under Compression," *Thin-Walled Structures*, vol. 76, pp. 145–156, Mar. 2014, doi: 10.1016/j.tws.2013.11.009.

[6] J. Leng, Z. Li, J. K. Guest, and B. W. Schafer, "Shape Optimization of Cold-Formed Steel Columns with Fabrication and Geometric End-Use Constraints," *Thin-Walled Structures*, vol. 85, pp. 271–290, Dec. 2014, doi: 10.1016/j.tws.2014.08.014.

[7] "Single Pile Mounting With Concrete Foundation." https://www.broadsolartek.com/single-pile-mounting-with-concrete-foundation_p25.html

[8] Z. Li and B. W. Schafer, "Buckling Analysis of Cold-Formed Steel Members with General Boundary Conditions Using CUFSM: Conventional and Constrained Finite Strip Methods," presented at the Twentieth International Specialty Conference on Cold-Formed Steel Structures, Saint Louis, MO, Nov. 2010.

[9] S. Ádány and B. W. Schafer, "Buckling Mode Classification of Members with Open Thin-Walled Cross-Sections," presented at the Fourth International Conference on Coupled Instabilities in Metal Structures, Rome, Italy, Sep. 2004.

[10] B. W. Schafer, "Advances in the Direct Strength Method of Cold-Formed Steel Design," *Thin-Walled Structures*, vol. 140, pp. 533–541, Jul. 2019, doi: 10.1016/j.tws.2019.03.001.

[11] B. W. Schafer, "Review: The Direct Strength Method of Cold-Formed Steel Member Design," *Journal of Constructional Steel Research*, vol. 64, no. 7–8, pp. 766–778, Jul. 2008, doi: 10.1016/j.jcsr.2008.01.022.

[12] C. Ding, "Strength and Behavior of Advanced High Strength Steel Structural Components," PhD Dissertation, Johns Hopkins University, Baltimore, MD, 2022.

[13] E28 Committee, "Test Methods for Tension Testing of Metallic Materials," ASTM International, Jul. 2013.

[14] X. Zhao, "Measurement and Application of Geometric Imperfections in Cold-Formed Steel Members," PhD Dissertation, Johns Hopkins University, Baltimore, MD, 2016.

[15] D. Akchurin, S. Torabian, C. Ding, and B. W. Schafer, "Compressive Capacity of Cold-Formed Steel High Strength Low-Alloy Lipped Channels with Intermediate Stiffeners," Johns Hopkins University, R-2023-1, Jan. 2023. [Online]. Available: https://jscholarship.library.jhu.edu/handle/1774.2/67817

[16] AISI Committee, *AISI S100-16: North American Specification for the Design of Cold- Formed Steel Structural Members*. American Iron and Steel Institute, 2016.